Multiple rare-earth ion environments in amorphous $(Gd_2O_3)_{0.230}(P_2O_5)_{0.770}$ revealed by gadolinium *K*-edge anomalous x-ray scattering

Jacqueline M. Cole,[1,2,3,4,*] Alisha J. Cramer,[1] Sarvjit D. Shastri,[3] Karim T. Mukaddem,[1] and Robert J. Newport[5]

[1]*Cavendish Laboratory, Department of Physics, University of Cambridge, J. J. Thomson Avenue, Cambridge CB3 0HE, United Kingdom*

[2]*ISIS Neutron and Muon Source, STFC Rutherford Appleton Laboratory, Harwell Science and Innovation Campus, Didcot, Oxfordshire OX11 0QX, United Kingdom*

[3]*Argonne National Laboratory, 9700 South Cass Avenue, Argonne, Illinois 60439, USA*

[4]*Department of Chemical Engineering and Biotechnology, University of Cambridge, West Cambridge Site, Philippa Fawcett Drive, Cambridge CB3 0FS, United Kingdom*

[5]*School of Physical Sciences, Ingram Building, University of Kent, Canterbury CT2 7NH, United Kingdom*

(Received 8 December 2017; published 26 April 2018)

A Gd *K*-edge anomalous x-ray scattering (AXS) study is performed on the rare-earth (*R*) phosphate glass, $(Gd_2O_3)_{0.230}(P_2O_5)_{0.770}$, in order to determine Gd $\cdots$ Gd separations in its local structure. The minimum rare-earth separation is of particular interest given that the optical properties of these glasses can quench when rare-earth ions become too close to each other. To this end, a weak Gd $\cdots$ Gd pairwise correlation is located at 4.2(1) Å, which is representative of a metaphosphate $R \cdots R$ separation. More intense first-neighbor Gd $\cdots$ Gd pairwise correlations are found at the larger radial distributions, 4.8(1), 5.1(1), and 5.4(1) Å. These reflect a mixed ultraphosphate and metaphosphate structural character, respectively. A second-neighbor Gd $\cdots$ Gd pairwise correlation lies at 6.6(1) Å which is indicative of metaphosphate structures. Meta- and ultraphosphate classifications are made by comparing the $R \cdots R$ separations against those of rare-earth phosphate crystal structures, $R(PO_3)_3$ and RP_5O_{14}, respectively, or difference pair-distribution function (ΔPDF) features determined on similar glasses using difference neutron-scattering methods. The local structure of this glass is therefore found to display multiple rare-earth ion environments, presumably because its composition lies between these two stoichiometric formulae. These Gd $\cdots$ Gd separations are well-resolved in ΔPDFs that represent the AXS signal. Indeed, the spatial resolution is so good that it also enables the identification of $R \cdots X$ ($X = R$, P, O) pairwise correlations up to $r \sim 9$ Å; their average separations lie at $r \sim 7.1(1)$, 7.6(1), 7.9(1), 8.4(1), and 8.7(1) Å. This is a report of a Gd *K*-edge AXS study on an amorphous material. Its demonstrated ability to characterize the local structure of a glass up to such a long range of *r* heralds exciting prospects for AXS studies on other ternary noncrystalline materials. However, the technical challenge of such an experiment should not be underestimated, as is highlighted in this work where probing AXS signal near the Gd *K* edge is found to produce inelastic x-ray scattering that precludes the normal AXS methods of data processing. Nonetheless, it is shown that AXS results are not only tractable but they also reveal local structure of rare-earth phosphate glasses that is important from a materials-centered perspective and which could not be obtained by other materials characterization methods.

DOI: 10.1103/PhysRevMaterials.2.045604

I. INTRODUCTION

Rare-earth phosphate glasses (REPGs) have shown great promise in the laser and optoelectronics industry [1–5]. This is because the rare-earth ions possess the required energy levels for achieving successful population inversion, and the nonlinear refractive index of the phosphate glass is large enough to exhibit the desired effects without causing beam breakup and damage. REPGs with stoichiometries $(R_2O_3)_x(P_2O_5)_{1-x}$, where x ranges from 0.167 (ultraphosphate) to $x = 0.25$ (metaphosphate), have shown particular promise. For example, silicon-clad optical fibers that have lasing capabilities have been furnished from the REPG $(Nd_2O_3)_{0.011}(La_2O_3)_{0.259}(P_2O_5)_{0.725}(Al_2O_3)_{0.005}$ [6]. Solid-state lasers containing the closely related tetraphosphate $LiEr_xYb_yLa_{(1-x-y)}P_4O_{12}$ glass have also been developed [7,8]. However, their lasing ability suffers from quenching in the presence of OH^- ions [7]. This contrasts with metaphosphate glasses that are much more stable to water, this being an important criterion when considering practical device applications.

Since the dopant rare-earth ions in REPGs with compositions ranging from ultra- and metaphosphate exist in such a high concentration (16.7−25% molar volume: R_2O_3), these materials have also been found to exhibit a multitude of exotic properties at low temperatures. For example, the onset of acoustic mode softening in these materials is observed at $T < 20$ K, resulting in negative thermal expansion coefficients [9] and bulk moduli [10], i.e., the material becomes easier to squeeze with the application of pressure or the lowering of temperature. The compounds also exhibit unprecedented magnetic, magneto-optical, and optoacoustic phenomena in this $T < 20$ K temperature region [11].

*Corresponding author: jmc61@cam.ac.uk

On account of this multitude of unusual properties, the atomic structure of REPGs with ultra- to metaphosphate stoichiometries has been studied extensively in order to relate structure to function. To this end, the atomic structure of a series of REPGs $(R_2O_3)_x(P_2O_5)_{1-x}$, where $x = 0.167-0.250$, and R = La, Ce, Pr, Nd, Sm, Eu, Gd, Tb, Dy, Ho, Er have been probed, using a range of conventional x-ray [12–19] and neutron [13,15,17,20] diffraction, rare-earth K-edge [21] and L_{III}-edge [12,22–24] x-ray absorption spectroscopy (XAS), ^{27}Al and ^{31}P solid-state NMR [14,20] and Fourier transform infrared [25] spectroscopy techniques. Combining the results from these experimental studies has afforded a model of the local atomic structure of these REPGs, which is comprehensive out to a radial distribution limit, $r \sim 3.8$ Å. Figure 1(a) illustrates the nature of this structure. Its core framework comprises a rigid network of regular PO_4 tetrahedra, whose oxygens bond to either P or R in a covalent (bridging) or ionic (terminal) fashion, respectively. The bridging oxygens (O_B) help forge cages or extended chains that make up the phosphate network [Fig. 1(b)]. The terminal oxygens (O_T) surround the R^{3+} ion which resides in a distorted octahedral geometry. The extent of this distortion is governed by the coordination number of R (N_{RO}), which ranges from 6 to 8 depending on both the REPG composition [16,18] and the size of the lanthanide ion [13–15,17] [Fig. 1(c)]. The greater N_{RO}, the greater this distortion, since regular octahedral geometry is depicted by sixfold coordination. The associated R-O separation ranges from ~2.2 to 2.5 Å, decreasing with increasing rare-earth atomic number, Z_R (decreasing R^{3+} ion size) as per the lanthanide contraction. The exact degree of contraction is influenced by the REPG composition, as illustrated in Fig. 1(d).

REPGs are typically fabricated using alumina crucibles, and in such cases a few wt% of these R^{3+} ion sites in REPGs are substituted by aluminum ions, as revealed by solid-state ^{27}Al NMR spectroscopy [20], and corroborated by neutron [20] and x-ray diffraction [14] data. The pair-distribution functions from these diffraction studies presented a small peak centered at $r = 1.8$ Å, which is characteristic of an Al-O separation. These studies also demonstrated that this few wt % of aluminum impurity is responsible for the high level of durability observed in these glasses, and yet it does not act as a network modifier. The ^{27}Al NMR spectroscopy revealed that Al^{3+} ions lie in one of the three (4-, 5-, or 6-coordinated) structural environments present within the overarching extended framework structure of these REPGs.

In addition to determining this directly bonded (first-neighbor) core structure of REPGs, second- and third-neighbor coordination shell structure has been sought using extended x-ray absorption fine-structure (EXAFS) spectroscopy and diffraction data. Both K- and L_{III}-edge EXAFS spectra [12,21–24] displayed a substantial amount of multiple scattering, which obscured the true structure from reliable interpretation beyond first-neighbor shell information. Diffraction data [12–20] fared rather better, affording a comprehensive structural model up to $r \sim 3.8$ Å, in the sense that every peak in the pair-distribution function could be assigned up to this radial limit. Beyond this value of r, there are too many overlapping atomic pairwise correlations to be able to distinguish individual peaks in the pair-distribution function.

It is notable that there is no $R \cdots R$ pairwise correlation present in this model, which means that the closest rare-earth separation must lie at $r > 3.8$ Å. This is a rather important omission in the model when considering the physical properties of these materials that we seek to understand, especially since optical properties are well known to quench when rare-earth ions become too close to each other. Yet, structural inquiry of REPGs had reached the technical limitations of conventional diffraction (overlapping correlations), K- and L_{III}-edge EXAFS spectroscopy (multiple scattering and damping effects) and solid-state NMR spectroscopy (inherent short-range J-J coupling effects and very broad signal, especially given the paramagnetic nature of all non-lanthanum-containing REPGs).

Given these limitations, Cole *et al.* have turned to more specialized materials characterization techniques in order to realize the closest $R \cdots R$ separations in this series of REPGs. To this end, they have hitherto reported two difference diffraction experiments: (a) a magnetic difference experiment where neutron scattering specific to the paramagnetism of terbium ions was exploited to draw out Tb $\cdots$ Tb structural signatures in a $(Tb_2O_3)_{0.246}(P_2O_5)_{0.722}(Al_2O_3)_{0.032}$ glass [26]; (b) an anomalous dispersion neutron-scattering study which exploits the energy-selective neutron-scattering cross section of Sm to draw out diffraction contributions in $(Sm_2O_3)_{0.205}(P_2O_5)_{0.795}$ that are exclusive to this element, and thus to Sm $\cdots$ Sm pairwise atomic correlations [27,28]. Broad structural signatures were obtained in each study but the closest $R \cdots R$ separations, on average, could nonetheless be identified at $r \sim 4.0$ Å. The composition of the former sample is close to meta-, while the latter is much closer to that of ultraphosphate. The results of these two studies therefore exemplified $R \cdots R$ separations at either side of the compositional range of our REPGs.

This paper seeks the $R \cdots R$ separation in a $(Gd_2O_3)_{0.230}(P_2O_5)_{0.770}$ glass, i.e., an example of a REPG with an intermediate composition within this ultra-to-metaphosphate range. For this purpose, we consider the exploitation of a third difference diffraction technique: anomalous x-ray scattering (AXS). The envisaged AXS results will need to be corroborated against the existing knowledge about $R \cdots R$ separations in rare-earth ultra- and metaphosphate glasses. Such knowledge is therefore first summarized along with a description of two specialist difference neutron-diffraction techniques that have been used to determine these $R \cdots R$ separations; their description is particularly important since they feature highly as comparative data for the scientific interpretation of the AXS results. The technical challenges of AXS are then described since they are not trivial. With these in mind, the experimental AXS study on $(Gd_2O_3)_{0.230}(P_2O_5)_{0.770}$ is described and the scientific results are presented.

We will show that the closest $R \cdots R$ separation lies at 4.2(1) Å and yet there are manifold first-neighbor $R \cdots R$ pairwise correlations in this glass that present with greater prominence at the larger radial distributions, 4.8(1), 5.1(1), and 5.4(1) Å. We will evidence that these multiple rare-earth

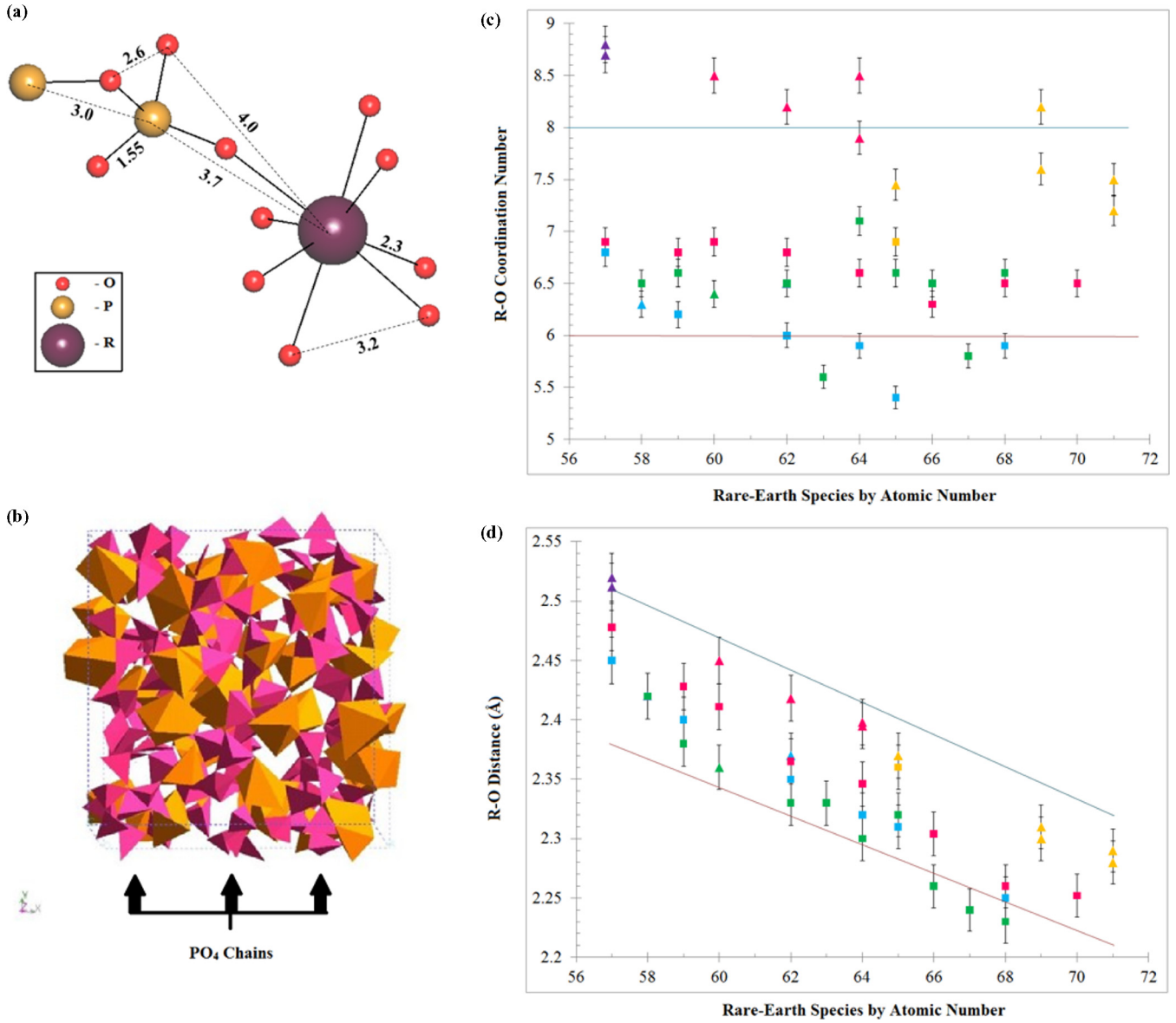

FIG. 1. Local structure of rare-earth (R) phosphate glasses, $(R_2O_3)_x(P_2O_5)_{1-x}$, showing its (a) modeled geometry up to a radial distribution of $r = 3.8$ Å; (b) extended chains of its phosphate network (pink: PO_4 tetrahedra; orange: RO_n polyhedra) taken from a reverse Monte Carlo model of a REPG [29]; (c) R-O coordination number, N_{RO}, as a function of atomic number Z_R, as determined by Cramer *et al.* [19] (cyan); Cole *et al.* [14] (green); Hoppe *et al.* [17] (red); Hoppe *et al.* [18] (yellow); Hoppe *et al.* [16] (purple); (d) first-neighbor R-O separation as a function of Z_R, as determined by Cramer *et al.* [19] (cyan); Cole *et al.* [14] (green); Hoppe *et al.* [17] (red); Hoppe *et al.* [18] (yellow); Hoppe *et al.* [16] (purple).

ion environments are indicative of a mixed ultra- and metaphosphate structural character, by relating the $R \cdots R$ separations to those in rare-earth phosphate crystal structures and difference pair distribution function (ΔPDF) features from two difference neutron-diffraction experiments on other REPGs. The technical merits of the AXS results will also be considered, and certain data processing and validation steps are highlighted, given that these are mandated by the presence of unexpected inelastic x-ray scattering. Given that this is a report of a Gd K-edge AXS study on an amorphous material, the prospects of applying AXS to determine selective local structure in other ternary noncrystalline materials are also discussed, especially in light of the excellent spatial resolution that these AXS results are found to impart.

II. COLLATED KNOWLEDGE ON $R \cdots R$ PAIRWISE ATOMIC CORRELATIONS IN RARE-EARTH PHOSPHATE GLASSES, $(R_2O_3)_x(P_2O_5)_{1-x}$ $(0.167 < x < 0.25)$

Before embarking on the subject of AXS study, it is important to consider all of the *a priori* evidence on $R \cdots R$ pairwise atomic correlations for this series of REPGs and to do so in a concerted fashion, in order to produce a consistent model. In a few instances, this involves a slight reinterpretation of some previous results, given the benefit of newer data to consolidate or improve upon initial hypotheses. The evidence presented comprises the results from the two aforementioned difference diffraction experiments, reverse Monte Carlo (RMC) studies, first sharp diffraction peaks manifesting in conventional

diffraction data, and reference $R\cdots R$ bond lengths from rare-earth ultra- and metaphosphate crystal structures.

We consider first the magnetic difference experiment performed on the $(Tb_2O_3)_{0.246}(P_2O_5)_{0.722}(Al_2O_3)_{0.032}$ glass [26]. This involved exploiting the paramagnetic nature of terbium ions, whereby the difference between low-temperature ($T = 4$ K) diffraction data with and without an applied magnetic field ($B = 4$ T) was acquired. This drew out $R\cdots R$ structural signatures in the corresponding pair-distribution function which were void of the usual overlapping peaks from other pairwise correlations that are seen in conventional diffraction data, since the nature of this difference nullifies nonmagnetic structural contributions. $R\cdots R$ separations centered at 3.9 and 6.4 Å were determined accordingly. These values aligned well with RMC simulations of terbium metaphosphate glass that indicated a closest $R\cdots R$ separation of 3.9 Å [29]. The magnetic difference diffraction and RMC simulations agreed in the assignment of this peak to an R-O_T-R bridging coordination. The RMC study also predicted a second-neighbor $R\cdots R$ separation of 5.4 Å; while this was not pinpointed explicitly in the magnetic difference experiment, the peak centered at 6.4 Å that Cole *et al.* reported was very broad, and modeled according to a Debye-Waller factor of 1.2 Å. So, the $R\cdots R$ separation of 5.4 Å predicted by the RMC simulations lies well within this tolerance, and is presumably present together with a range of other $R\cdots R$ separations to account for the peak breadth. Mountjoy and co-workers also performed a molecular-dynamics study on terbium metaphosphate glass [30] and found a small peak at ∼4 Å together with the main peak which is very broad, centering at ∼6 Å; this registers as the second-neighbor $R\cdots R$ correlation. These relative peak intensities reflected those of the aforementioned magnetic difference diffraction study. Both studies assigned the main peak to an R-(OPO)-R coordination, i.e., the majority of rare-earth ions are bridged by a PO_4 unit in terbium metaphosphate glass.

It is important to compare structural studies that feature the same rare-earth ion and REPG compositions, given the intricate relationship between the size of a rare-earth ion and the REPG composition [cf. Figs. 1(c) and 1(d)]. Nonetheless, it is also worth mentioning a conventional diffraction study by Hoppe *et al.* [17], who interpreted first sharp diffraction peaks to offer indirect experimental evidence for the second-neighbor $R\cdots R$ correlation in rare-earth metaphosphate glasses whose R-ion size spans the lanthanide series (albeit incompletely, not including terbium). Their results suggested that second-neighbor $R\cdots R$ correlations in REPGs with metaphosphate composition vary from 6.4 to 6.0 Å from La to Yb, respectively. These findings are entirely consistent with the results of the magnetic difference diffraction study and RMC simulations on terbium metaphosphate glass.

Having captured the structural signature of $R\cdots R$ correlations for a rare-earth metaphosphate glass for a small R^{3+} ion (high Z_R), Cole *et al.* sought for possible variation of $R\cdots R$ separations in REPGs whose composition lies between meta- and ultraphosphate. This led them to perform the second type of difference diffraction experiment comprising a complete anomalous neutron-scattering study on an amorphous material [27,28]. This technique exploits the wavelength-dependent variation in the real $[b'(\lambda)]$ and imaginary $[ib''(\lambda)]$ terms of the neutron-scattering length (b) of samarium, in the region of its absorption resonance. The summation of these anomalous dispersion terms with the wavelength-independent neutron-scattering length b_0 corresponds to the total neutron-scattering length; i.e.,

$$b_{Sm} = b_0 + b'(\lambda) + ib''(\lambda). \quad (1)$$

Samarium is one of the few elements in the periodic table which has an isotope (^{149}Sm) with an absorption resonance that displays sufficient neutron-scattering contrast within an accessible energy range that makes it amenable to this method [31]. Moreover, the case for samarium is sufficiently favorable that a sample without ^{149}Sm isotopic enrichment can be used for such experiments [28] (^{149}Sm is 14% naturally abundant in samarium).

The sample studied was a $(Sm_2O_3)_{0.205}(P_2O_5)_{0.795}$ glass, i.e., bearing a composition that lies between meta- and ultraphosphate, and yet is distinctly closer to ultraphosphate. Sm$\cdots$Sm correlations could be obtained exclusively by contrasting the differences in neutron-diffraction data between data acquired at wavelengths close to and far from the absorption resonance of samarium, where λ is judiciously chosen such that $b''(\lambda)$ is varied while $b'(\lambda)$ is kept constant and vice versa. This yields the difference correlation, $\Delta T''(r)$.

The first-neighbor Sm$\cdots$Sm pairwise correlation revealed by $\Delta T''(r)$ consists of a broad asymmetric peak, centered at 4.8 Å, whose full width at half maximum ranges from ∼4.0 to 5.2 Å. The asymmetry manifests on the low-r side of the peak, and suggests the presence of a smaller, underlying peak at around 4.0 Å. A similarly weak peak was found at this value of r in the magnetic difference study on terbium metaphosphate, as discussed above. This indicates that 4.0 Å is the closest Sm$\cdots$Sm separation in this REPG and that this peak signature corresponds to a rare-earth environment whose local structure is characteristic of a metaphosphate glass. This closest Sm$\cdots$Sm separation relates well to the minimum Sm$\cdots$Sm distance anticipated in crystalline samarium metaphosphate, SmP_3O_9, whose crystal structure [32] is isomorphous to that of NdP_3O_9 which, in turn, exhibits a minimum $R\cdots R$ separation of 4.234 Å [33]. This Sm$\cdots$Sm contact corresponds to Sm–(O_T)–Sm bonding.

The overarching broad and strong nature of this first-neighbor correlation suggests that the samarium glass in fact comprises multiple Sm$\cdots$Sm correlations. Substantial levels of static disorder in the Sm–(O_T)–Sm bonding could account for some, but not all, of this peak breadth. Based on the first-neighbor Sm-O distance [2.375(5) Å] in the sample, determined from this same study, the maximum Sm-(O)-Sm separation would be double this value, whereby the Sm-$\widehat{O}$-Sm angle subtends 180°, i.e., 4.75 Å. The structural signature that lies beyond 4.75 Å within the overarching broad correlation (∼ 4.75−5.2 Å) must therefore correspond to a second-neighbor Sm$\cdots$Sm correlation. Considering that the sample composition of this glass lies between that of meta- and ultraphosphate, possible Sm$\cdots$Sm structural signatures within this ∼4.75−5.2 Å range were compared against those from reference samarium meta- *and* ultraphosphate crystal structures. It transpires that the minimum Sm$\cdots$Sm separation

in the crystal structure of samarium ultraphosphate, SmP_5O_{14}, is 5.175 Å [34]. This compares favorably with this range observed for the samarium glass, but it is in stark contrast to the much shorter $R \cdots R$ contact in crystalline samarium metaphosphate that closely aligns with the aforementioned minimum correlation of this glass at ∼4 Å. Hence, it would appear that $(Sm_2O_3)_{0.205}(P_2O_5)_{0.795}$ glass could consist of rare-earth environments whose local structure is a mixture of ultra- and metaphosphate characteristics.

Indeed, the overall profile of the difference $R \cdots R$ correlation in this samarium study differs markedly from the magnetic difference study on the terbium glass where r lies beyond ∼4 Å. This difference corroborates the notion that REPGs with compositions between those of ultra- and metaphosphate (e.g., the samarium glass) display a mixture of rare-earth environments, while those that closely resemble metaphosphate (e.g., the terbium glass) present only one type of rare-earth environment. Moreover, since the composition of this samarium glass is closer to ultraphosphate than metaphosphate, the ultraphosphate structural signatures will presumably be more prominent. Indeed, the peak centered at 4.0 Å is indicated in the samarium study but it is not resolvable, unlike that of the terbium metaphosphate glass study.

With these results in hand, it seemed pertinent to establish the local structure of an REPG whose composition lay on the other side of the median of ultra- and metaphosphate, relative to that of the samarium glass. To this end, a study on $(Gd_2O_3)_{0.232}(P_2O_5)_{0.768}$ was of interest. For this work, a third type of difference diffraction experiment was employed: anomalous x-ray scattering.

III. ANOMALOUS AXS: METHOD AND CHALLENGES

The AXS technique is essentially analogous to that of the anomalous neutron-scattering method presented above. Wavelength-dependent real $[f'(\lambda)]$ and imaginary $[f''(\lambda)]$ terms of the atomic scattering factor, f, present anomalous scattering contributions to the overall x-ray scattering when diffraction studies are conducted in the vicinity of the x-ray absorption edge of one of the elements (R) in a sample under study. These anomalous scattering contributions augment the wavelength-independent Thomson scattering factor, f_0, to afford the overall atomic scattering factor for x-ray diffraction, i.e.,

$$f_R = f_0 + f'(\lambda) + if''(\lambda). \tag{2}$$

The difference between x-ray diffraction data collected at two x-ray energies, one on and one far from the x-ray absorption edge of the element of interest (R) within a sample, affords exclusively the anomalous scattering contributions of R. These present as pairwise $R \cdots X$ (X = any element) correlations for an amorphous material.

The application of AXS methods to amorphous materials was originally suggested by Krogh-Moe [35]. Such studies have since been borne out successfully on a range of glasses [36–39], solutions [40–43], amorphous alloys [44,45], and nanoparticles [46] using synchrotron-based x-ray diffraction. There are not so many AXS studies on amorphous materials as one might naively expect, considering Krogh-Moe's suggestion was reported in 1966 [35]. This is largely because the method remains technically challenging, even considering the latest advances in synchrotron radiation technology.

Since AXS is a difference diffraction method, errors in the data collected at a pair of x-ray energies sum in quadrature once one diffraction signature has been subtracted from the other. AXS will therefore pose signal-to-noise issues for any type of diffraction data. The inherently diffuse x-ray scattering associated with amorphous materials exacerbates this signal-to-noise problem. The use of large sample sizes to maximize x-ray scattering intensity can only help up to a point, since problems associated with sample attenuation and multiple scattering effects become more significant as the sample thickness increases. The availability of high-energy x rays, provided by the latest generation of synchrotron technology, can offset this problem to a certain degree. AXS difference data intensities are nonetheless inherently limited, given that the contrast ratio between atomic scattering factors f at two x-ray energies, one on and one far from the x-ray absorption edge probed, carries an essentially fixed maximum. The use of x-ray absorption edges of elements with high atomic number will tend to yield higher contrast ratios, given that f'' relates to the atomic absorption coefficient μ_a and the x-ray energy E, according to the optical theorem [47]:

$$f'' = \frac{m_e c \varepsilon_0 E}{e\hbar}\mu_a, \tag{3}$$

where m_e is the mass of the electron, c is the speed of light, ε_0 is the dielectric constant, e is the charge of an electron, $\hbar$ is $h/2\pi$ where h is Planck's constant.

f' and f'' are also related via a Kramers-Kronig transformation [48,49]:

$$f' = \frac{2}{\pi}\int_0^\infty \frac{E' f''(E')}{E^2 - E'^2} dE'. \tag{4}$$

This shows that the largest f' values will be obtained in cases where the energy difference between the pair of x-ray diffraction measurements comprising an AXS experiment is maximized. X-ray absorption K edges are therefore favored for AXS experiments since they offer the highest possible energy for an x-ray absorption edge of a given element, assuming there is no interference from other x-ray absorption edges in this energy regime.

The determination of reliable f' values has presented a challenge for AXS data analysis. Indeed, theoretical values of f' are employed for the majority of AXS studies. These lack accuracy because f' is highly dependent on the chemical and electronic environment of the absorbing element; errors in f' on the order of 14% have been reported [50]. Yet, one cannot entirely measure f' experimentally. The closest one can come to an experimental derivation of f' is to measure f'' experimentally from x-ray absorption data and derive f' values from f'' using the Kramers-Kronig transformation shown above. This method is experimentally limited since f' relates to f'' via an improper integral in this transformation; yet, the f' values derived from f'' are defined within the necessarily finite energy range of the experimental data on f''. As such, f' values need to be extrapolated outside of this energy range from zero to infinity. High-energy extrapolation within the x-ray regime

is well known to be problematic up to about 34 keV, beyond which the simple power law, $1/\omega^4$ in frequency, ω, is judged to apply well [51]. AXS experiments that probe elements of sufficiently high atomic number that their x-ray absorption K edge lies above 34 keV would therefore seem to offer the most tractable structural results.

A more technical challenge that has faced AXS experiments relates to the issue that x-ray data contain scattering contributions from several distinct phenomena, from which it can be difficult to distinguish the AXS data sought. To this end, x-ray diffraction data acquired in the vicinity of an x-ray absorption edge will generally contain elastic scattering (AXS signal), K_α and K_β x-ray fluorescence, and Compton scattering. Energy-discriminating detectors can distinguish these scattering contributions from the total signal, as long as they can resolve K_β fluorescence, Compton scattering, and elastic scattering signals, which tend to be near-coincident in energy. Fortunately, K_α fluorescence is usually well separated in energy from these other scattering contributions. Given this, K_α can be measured and used together with its inherent relationship with K_β, in terms of *a priori* known K_α/K_β ratios, to help extract the K_β component from the elastic and Compton scattering [52,53]. The detector must also display good counting statistics, bearing in mind that the elastic scattering intensity may only comprise ~10% of the total detector signal [54] while the AXS contribution therein can easily be $\sim 100^{\text{th}}$ of the elastic scattering intensity [37]. However, good statistics must not be compromised to the extent that the detector dead time becomes so long that a nonlinear detector response results [37,39,54].

The subject material presents a good case study for the application of AXS on several accounts. Firstly, the study requires probing anomalous scattering contributions at the Gd K edge whose energy (50.252 keV) [55] lies well above the threshold x-ray energy of 34 keV where f' values can be extrapolated reliably from the simple power law, $1/\omega^4$ [51]. Measurable f'' values are also available for this study via Gd K-edge EXAFS data that have been collected previously on this REPG [21]. It therefore stands to be possible to overcome the aforementioned AXS challenge in producing reliable f' and f'' values. A strategy to overcome the more technical challenge of separating AXS signal from other scattering signatures with similar energies is more difficult to define and implement, but with good detectors and careful data processing, this is possible.

The nature of the AXS method will afford ΔPDFs by subtracting a data set with an x-ray energy far from the Gd K edge from that of one on the Gd K edge. These ΔPDFs will feature exclusively $R \cdots X$ (X = any element) atomic pairwise correlations. The fact that the subject glass contains three elements, i.e., it is a ternary glass, presents this AXS study with an interesting additional material challenge since AXS studies on glasses have generally been confined to binary materials [36,38,39]. The one exception [37] was coincidentally a study on a metal phosphate glass, $Eu_{0.1}Sr_{0.9}(PO_3)_2$, although that study did not present detailed data analysis on the material. Rather, it used the sample primarily to test the AXS experimental setup of the synchrotron beam line that was the focus of that work.

IV. AXS EXPERIMENT AND DATA ANALYSIS

A. Sample preparation

The $(Gd_2O_3)_{0.232}(P_2O_5)_{0.768}$ sample was synthesized using the method described by Mierzejewski *et al.* [56]. This comprised heating a 1:4 ratio of high-purity (99.9%) rare-earth oxide and P_2O_5 in an aluminum oxide crucible to the temperature of the gadolinium oxide melt, followed by annealing. All raw chemicals were obtained from Sigma-Aldrich and used without further purification. The sample composition was determined by electron probe microanalysis while the bulk density measurements used the Archimedes principle via a measure of the weight of the sample in both air and water [57]. The sample contains a small amount of Al_2O_3 impurity (1–2 wt% Al), arising from the crucible used in sample preparation, which improves its ductility [20].

B. AXS experiment

A 0.5 mm thick disk of finely powdered $(Gd_2O_3)_{0.232}(P_2O_5)_{0.768}$ sample was held within an aluminum annulus and between two Kapton windows; the assembly was mounted onto a six-circle diffractometer in flat-plate geometry. This diffractometer was housed on the synchrotron beam line, 1-BM, at the Advanced Photon Source, Argonne National Laboratory, Illinois, USA. X rays were delivered to the instrument via a Si(400) crystal monochromator and they were detected using an energy-dispersive germanium detector. X-ray slits were optimized so as to afford a 0.1 $Å^{-1}$ resolution with a usable dynamic range, $Q = 0.4{-}30\ Å^{-1}$, where $Q = 4\pi(\sin\theta)/\lambda$. Two ion chambers were installed either side of the primary slits to ensure that they are in an optimum position with respect to the incident beam. The post-slit ion chamber also acts to normalize photons on the sample. Diffraction scans were performed using $2\theta/\theta$ geometry at four x-ray energies: 10, 40, 300, and 500 eV below the gadolinium K edge (50.239 keV), which was calibrated using a gadolinium foil. Single-channel analyzers were used to optimize the energy range of the multichannel analyzer (MCA) detector, prior to these scans, in order to ensure that the different scattering contributions to the signal (elastic, K_α, and K_β fluorescence, and Compton scattering) were all included while minimizing noise levels. The detector integrated 7.5–12 million counts per data point at each 0.1 $Å^{-1}$ step-scan increment and duplicate scans were acquired for data corresponding to the larger dynamic range, $Q = 10{-}30\ Å^{-1}$, which were subsequently averaged, to produce good counting statistics across the entire dynamic range. The pixels of the MCA of the Ge detector were calibrated using a ^{109}Cd spectrum for reference. The full width at half maximum energy resolution of the Gd detector was 620 eV. The dead time of the detector was measured by fully opening the x-ray slits and comparing scans that record 6 million counts per data point in 0.1 $Å^{-1}$ increments across the range $Q = 0{-}2.5\ Å^{-1}$, with and without substantial attenuation between the two ion chambers that precede the sample area. This yielded a dead time on the order of 10 μs.

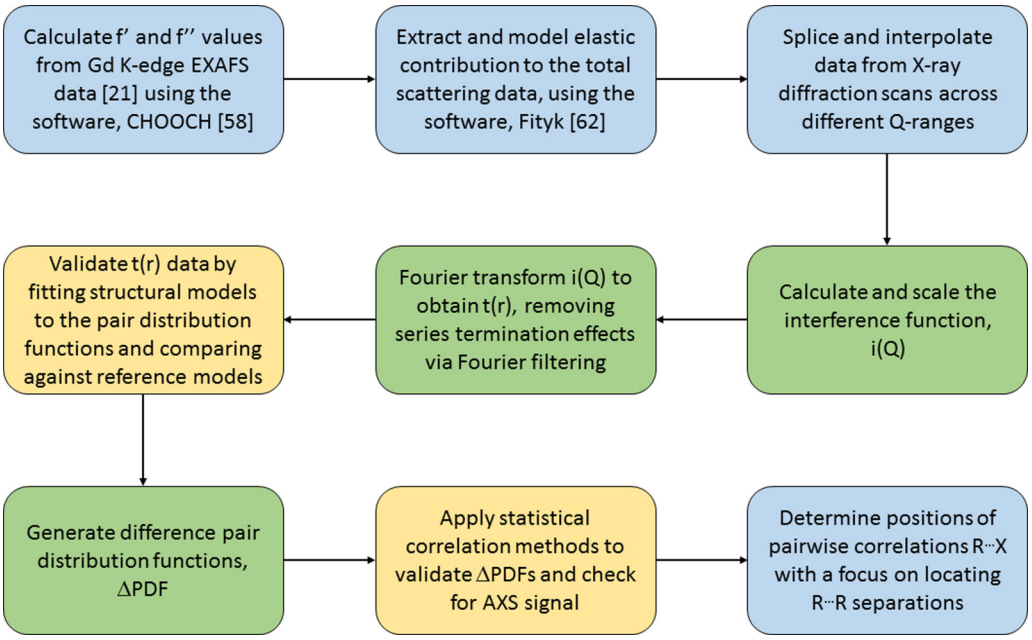

FIG. 2. Summary of the data-processing workflow for this Gd K-edge anomalous x-ray scattering study on $(Gd_2O_3)_{0.230}(P_2O_5)_{0.770}$. Boxes shaded in blue show steps that are specific to the AXS aspect of the data; those in yellow highlight key data validation steps for this AXS data treatment; those in green represent data-processing steps that are commonly applied to conventional diffraction data.

C. Data analysis

The overarching data analysis workflow is summarized in Fig. 2, while the details of the more complicated individual steps are contained within the following sections.

1. Determining the anomalous contributions (f' and f'') to the x-ray atomic scattering factor of gadolinium at the K edge

The f' and f'' values used in this data analysis were determined using the program CHOOCH [58]. This used experimental values of f'' in the vicinity of the Gd K edge that were taken from x-ray absorption spectroscopy measurements on a gadolinium phosphate glass with very similar composition to the subject sample: $(Gd_2O_3)_{0.229}(P_2O_5)_{0.771}$. These data were collected on the BM29 beam line at the European Synchrotron Radiation Facility, as reported previously [21], and converted into f'' via Eq. (3). These experimentally sourced f'' values were normalized against calculated values that were used to model an extended energy range, far from the Gd K edge. f' values were then derived from f'' using the Kramers-Kronig transformation shown in Eq. (4). CHOOCH was also used for this process, and employed the list of x-ray cross sections tabulated by McMaster *et al.* [59] as markers for the high-energy extrapolation to enable this improper integral to be evaluated. These tabulated values for gadolinium align well with the $1/\omega^4$ power law for high-energy extrapolation that is considered to be appropriate for energies higher than 34 keV [51].

2. Distinguishing the elastic scattering from Compton scattering and fluorescence contributions

As was discussed in the last section, the contribution of the elastic signal to the total x-ray scattering must be separated from those owing to Compton scattering and K_β fluorescence. To that end, K_α values and the K_β/K_α ratio are normally used to determine and thence subtract out the K_β contribution. The relative intensities of K_α and K_β are available from reference data [60], while an absolute value of K_α is measured via the $K_{\alpha1}$ and $K_{\alpha2}$ characteristic lines which present together as isolated signal, being markedly lower in energy than that of K_β, Compton, and elastic scattering. For example, consider the case study: $K_{\alpha1}$ and $K_{\alpha2}$ for Gd are 42.996 and 42.309 keV, respectively [61]; cf. the overlapping x-ray signatures of $K_{\beta1}$, $K_{\beta2}$, and $K_{\beta3}$, 48.697, 49.959, and 48.555 keV, which lie close to the Gd K edge (50.252 keV) [55]. However, while this approach would have presented the normal course of action for this AXS study, a complication arose in the data that precluded a reliable direct determination of K_α: a range of unexpected features in the x-ray signal presented at energies which overlapped with the energy range of K_α. These features were found to be energy dependent and appear to arise from a form of inelastic x-ray scattering. Fortunately, the energy of the detector was well calibrated for this experiment, and the elastic peak dominates the total scattering. So, it was possible to circumvent this problem by discriminating the elastic contribution directly from the total scattering by first using its peak intensity to define the center point of the elastic scattering contribution and then using the shape of the top of the peak to model the elastic scattering profile. This fitting was applied as a function of Q, using the program FITYK [62].

3. Producing pair-distribution functions and validating them at each x-ray energy

Having extracted the elastic profiles from the total scattering, atomic (nonbonding) scattering contributions were removed from the data, which were then scaled to generate an interference function $i(Q)$ [Eq. (5)] for each x-ray energy probed: 10, 40, 300, and 500 eV below the Gd K edge. These energies are hereafter known as K-10 eV, K-40 eV, K-300 eV,

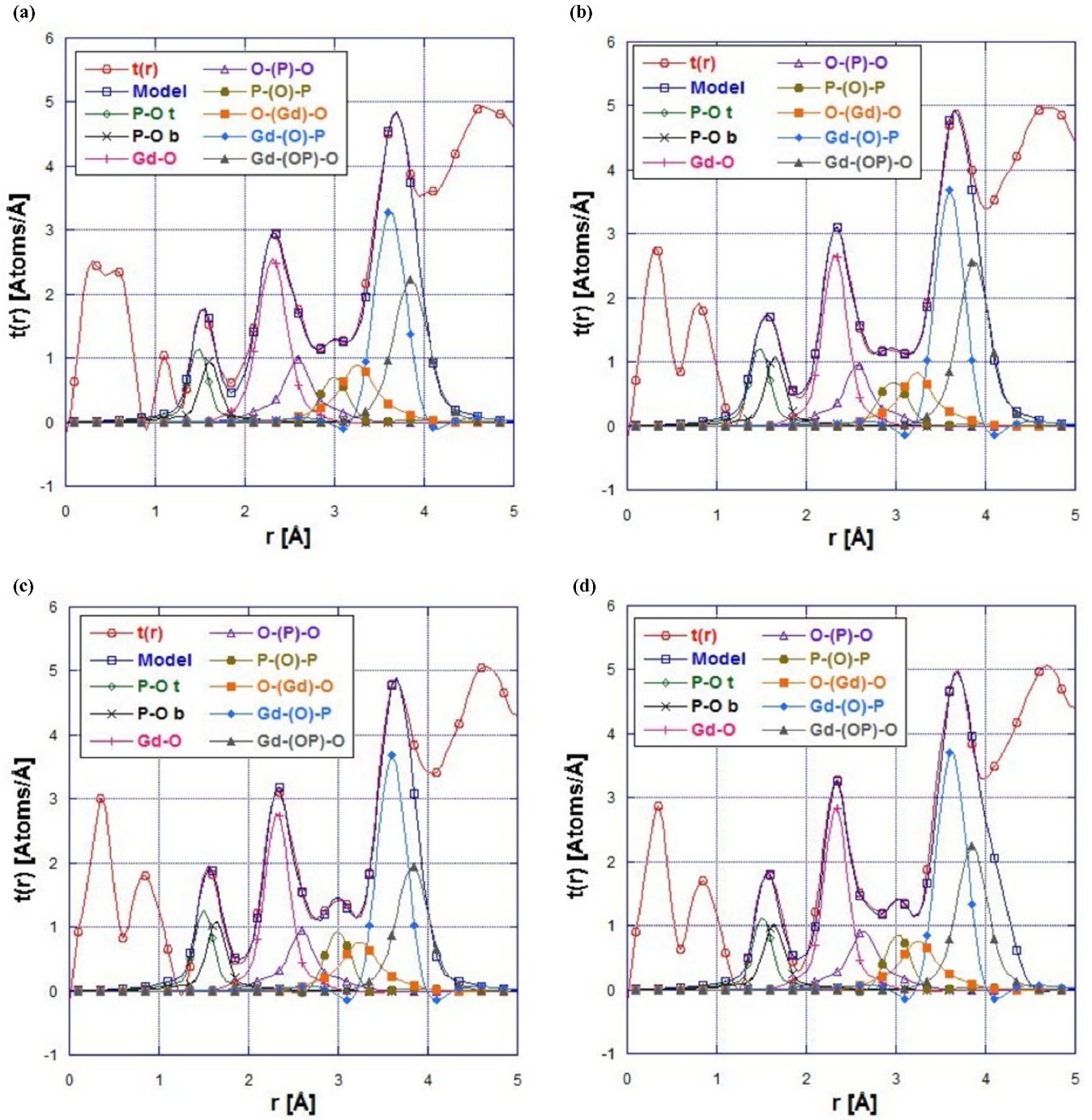

FIG. 3. Pairwise correlations of $(Gd_2O_3)_{0.230}(P_2O_5)_{0.770}$ modeled onto the pair-distribution functions of the four x-ray diffraction data sets collected at (a) 10, (b) 40, (c) 300, and (d) 500 eV from the Gd K edge. The local structure determined by these model fits to the data reproduce well a previous structural model of this REPG that was characterized by an independent conventional diffraction experiment [14], thus confirming that these data sets are of good quality.

and K-500 eV, respectively.

$$i(Q) = \frac{I_{\text{exp}} - (\langle f^2 \rangle + I_c)}{f^2 \bar{z}^2}, \tag{5}$$

where I_{exp} is the corrected experimental intensity, I_c is the normalized sum of the relative Compton contributions from each atom type, $\langle f^2 \rangle$ is the sum of the relative contributions of the square of the self-scattering factor from each atom type, $\langle f \rangle^2$ is the sum of the square of the relative contributions of the self-scattering factor from each atom type, and $\bar{z}^2$ is the mean number of electrons in a normalized scattering unit. These $i(Q)$ functions were then Fourier transformed to $t(r)$:

$$t(r) = 2\pi^2 r \rho_0 - \int_{Q_{\text{min}}}^{Q_{\text{max}}} Q i(Q) \sin(Qr) dQ. \tag{6}$$

This Fourier transform process used a Hanning window to reduce series termination errors and a $Q_{max} = 30\,\text{Å}^{-1}$. Fourier filtering was also applied to the K-10 eV data set since it displayed noticeable signal in the unphysical low-r region of $t(r)$. This filtering process had no effect on the data in the range of scientific interest, as verified by comparisons of $i(Q)$ with that of reverse Fourier-transformed $i(Q)$, and checks in $t(r)$ before and after the filtering process. Thus, this signal was taken to be an artifact associated with the x-ray energy of the data being so close to the inflection of the Gd absorption K edge; one might suspect Compton effects to be the most likely source of this signal since such scattering is most significant at high Q (low r). It has found to be structured in these data sets (e.g., in the K_α region) rather than manifest as a broad signature, and its removal from the elastic signal may not have been perfect especially in the energy region where there is already core-hole lifetime broadening effects that are particularly significant for a K edge associated with a heavy element, such as Gd.

The veracity of the resulting pair-distribution functions at each of the four x-ray energies was then checked by fitting atomic pairwise correlations to each individual peak in the $t(r)$ profiles up to $r \sim 4\,\text{Å}$, using the approach of Gaskell [63] for modeling. The structural parameters associated with these correlations (atomic separation R_{ij}, coordination number N_{ij}, and Debye-Waller factor σ_{ij}^2) are *a priori* known for this range of r, given that they have been modeled previously via conventional diffraction data [12–20]. These previous results thus served as independent reference values to compare against those generated from the PDFs herein, in order to test the robustness of the subject data. All structural parameters were well reproduced (see Fig. 3), except for the Gd-(OP)-O correlation, whose $R_{Gd(PO)O}$ value was consistently $0.15-0.24\,\text{Å}$ shorter than the reference value across the PDFs from all four x-ray energies. However, an inconsistency in this particular atomic pairwise correlation is not entirely surprising, considering that it lies at the extremity of r, in what can be modeled by

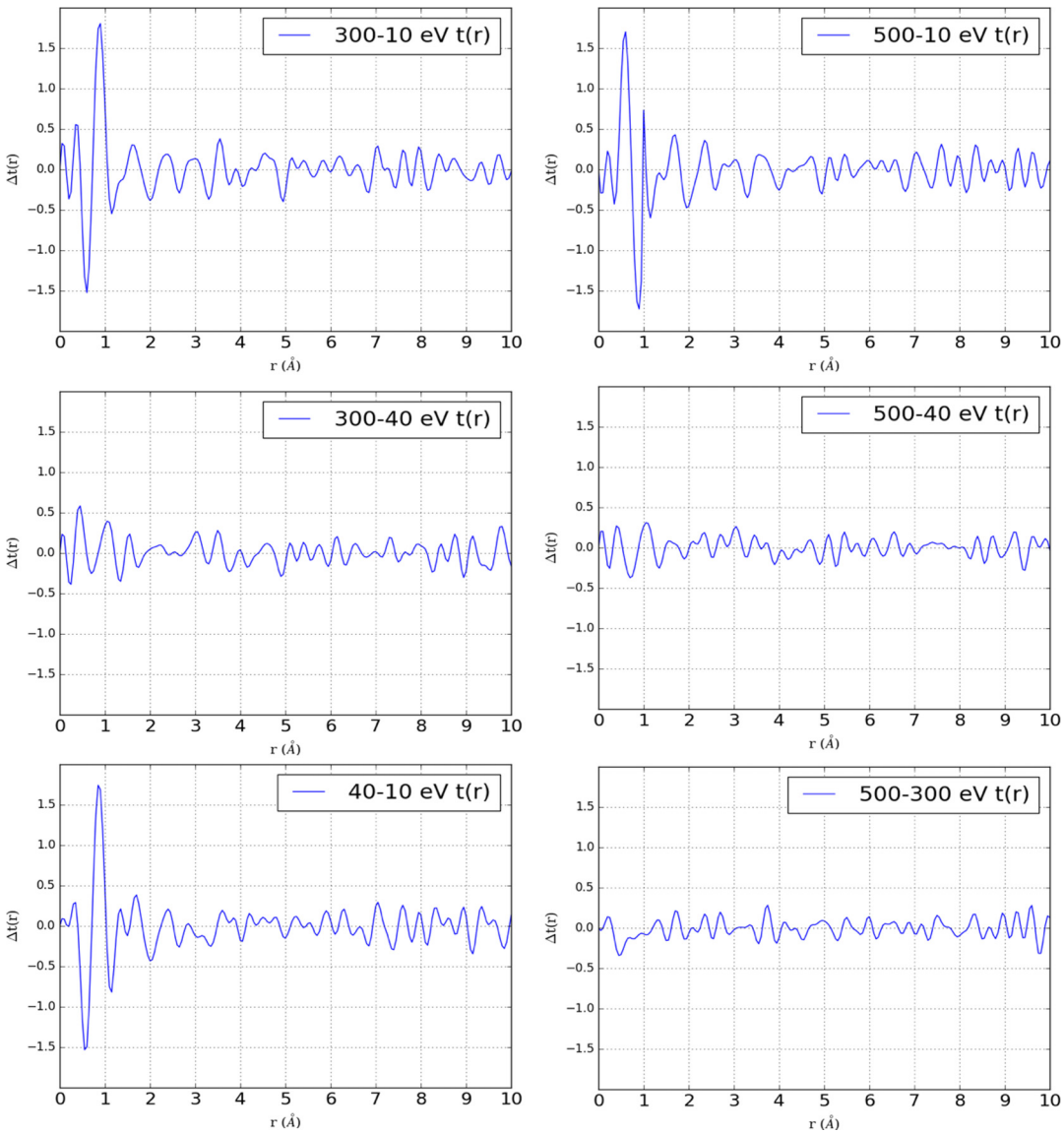

FIG. 4. All six possible ΔPDFs created by taking the difference between each unique pair of diffraction data sets on $(Gd_2O_3)_{0.230}(P_2O_5)_{0.770}$ collected at the four x-ray energies.

conventional x-ray diffraction. The veracity of the subject data was therefore borne out.

4. Validating difference pair-distribution functions: Checking for AXS signal

Having confirmed the veracity of the PDF data at each x-ray energy, difference pair-distribution functions were produced for all six possible pairs of x-ray energies. Such pairings enabled a validation of the self-consistency of AXS signal within the PDF. For example, the largest AXS contribution should arise in a ΔPDF produced by the subtraction of a PDF associated with an x-ray energy far from the Gd K edge from the one whose energy lies closest to this edge, i.e., maximizing $\Delta f(\lambda)$. Given the four x-ray energies where data were acquired, PDF[(K-300 eV)–(K-10 eV)] and PDF[(K-500 eV)–(K-10 eV)] should show the largest AXS contributions and thus the most noticeable $R \cdots X$ correlations; these two difference pairs should show comparable results given that 300 and 500 eV are sufficiently far from the Gd K edge that $\Delta f(\lambda) = 0$ in each case. Conversely, the ΔPDF corresponding to PDF[(K-500 eV)–(K-300 eV)] should essentially feature "noise" since $\Delta f(\lambda) = 0$ between these two data sets. ΔPDFs that involve x-ray data taken 40 eV from the Gd K edge are anticipated to show a discernible $\Delta f(\lambda)$, albeit a much more modest amount than that owing to the data collected 10 eV from the edge. So, ΔPDFs generated from PDF[(K-300 eV)–(K-40 eV)] and PDF[(K-500 eV)–(K-40 eV)] should show comparable results, where the AXS signal is less intense than that of cognate differences involving the K-10 eV data set. Meanwhile, the PDF[(K-40 eV)–(K-10 eV)] may result in a small AXS signal given that $\Delta f[(K\text{-}40\,\text{eV}) - (K\text{-}10\,\text{eV})] \neq 0$ but it is less than $\Delta f[(E_{\text{far from edge}}) - (K\text{-}10\,\text{eV})]$, where $E_{\text{far from edge}} = (K\text{-}300\ \text{eV})$ or $(K\text{-}500\ \text{eV})$, which will exhibit the maximum possible AXS signal. Indeed, these systematic expectations are borne out by observation, cf. simple visual inspection of overlays of ΔPDFs arising from different x-ray energies (Fig. 4).

Statistical correlation indexes were nonetheless employed to provide a quantitative basis for this observation. To this end, statistical correlations between all possible pairs of ΔPDFs were calculated using three figures-of-merit: Pearson, Spearman, and Kendall rank coefficients [64]. Data for these calculations were restricted to the range $r = 2{-}7$ Å. Below this range only noise is expected, by virtue of no possible $R \cdots X$ correlations manifesting between $r = 0{-}2$ Å. Above $r = 7$ Å, a sufficiently large number of $R \cdots X$ correlations will exist that their overlap will render them nonresolvable; also, statistical noise will already be significant in data at $r \sim 7$ Å or beyond, and both of these problems will only worsen as a function of increasing r. If AXS signal (from $R \cdots X$ correlations) is present in both of the ΔPDF signatures, these established statistical qualifiers should afford positive coefficients, the strength of which will be depicted by the range $0 \leqslant x \leqslant 1$ where 1 represents a perfect correlation; no AXS signal in both data sets should yield a zero; negative coefficients signify a level of anticorrelation up to a maximum of −1.

The results of these calculations are given in Table I. All three sets of coefficients are consistent in their trends, with the Pearson coefficients demonstrating slightly stronger trends than the other two metrics, judging from their slightly higher values overall.

TABLE I. Statistical correlations between ΔPDF signatures, calculated in the range $r = 2{-}7$ Å, using Pearson, Spearman, and Kendall rank coefficients; these three figures-of-merit range between 1 and −1 for pure correlation and anticorrelation, respectively, while 0 presents a null correlation.

	40–10 eV	300–10 eV	500–10 eV	300–40 eV	500–40 eV	500–300 eV
			Pearson coefficients for 2–7 Å region			
40–10 eV	*n/a*	0.704	0.724	−0.184	−0.221	−0.027
300–10 eV		*n/a*	0.832	0.568	0.299	−0.369
500–10 eV			*n/a*	0.311	0.511	0.208
300–40 eV				*n/a*	0.671	−0.479
500–40 eV					*n/a*	0.328
500–300 eV						*n/a*
			Spearman coefficients for 2–7 Å region			
40–10 eV	*n/a*	0.619	0.618	−0.218	−0.257	−0.047
300–10 eV		*n/a*	0.795	0.582	0.322	−0.362
500–10 eV			*n/a*	0.355	0.544	0.194
300–40 eV				*n/a*	0.671	−0.443
500–40 eV					*n/a*	0.307
500–300 eV						*n/a*
			Kendall rank coefficients for 2–7 Å region			
40–10 eV	*n/a*	0.449	0.446	−0.140	−0.182	−0.040
300–10 eV		*n/a*	0.613	0.410	0.210	−0.259
500–10 eV			*n/a*	0.240	0.370	0.126
300–40 eV				*n/a*	0.483	−0.305
500–40 eV					*n/a*	0.211
500–300 eV						*n/a*

The largest observed positive correlation is between the data, ΔPDF [(K-500 eV)–(K-10 eV)] and ΔPDF [(K-300 eV)–(K-10 eV)], as expected given that these pairs of ΔPDFs issue the same maximum possible AXS signal of all data sets, by virtue of having in common the K-10 eV data set, which possesses the greatest $\Delta f(\lambda)$ value, and the K-300 eV and K-500 eV data counterparts which are comparable since both of their x-ray energies are sufficiently far from the Gd K edge that $\Delta f(\lambda) = 0$. The statistical correlation that places second highest in rank order of coefficients for each of the three figures-of-merit is, on average, that pertaining to the relation between the data, ΔPDF [(K-300 eV)–(K-40 eV)] and ΔPDF [(K-500 eV)–(K-40 eV)], i.e., the same comparative data as the highest statistical correlation found, except that the K-40 eV data replace the K-10 eV data in each ΔPDF. This rank order makes sense once two factors have been considered: firstly, while $\Delta f(\lambda)$ will be lower for the K-40 eV data set than that for K-10 eV, it will not be zero, and yet $\Delta f(\lambda)$ will be zero for both K-300 eV and K-500 eV data sets; secondly, each ΔPDF component of this correlation will be comparable in signal given that $\Delta f(K\text{-}300\,\text{eV}) = \Delta f(K\text{-}500\,\text{eV}) = 0$, and the strength of the statistical correlations employed herein is based on not only signal intensity between ΔPDFs but also on the relative values of the ΔPDF signals, the more comparable values affording higher statistical correlation. The third and fourth highest ranked correlations relate closely to each other in that they both feature ΔPDF [(K-40 eV)–(K-10 eV)] whose two counterparts are ΔPDF [$E_{\text{far from edge}}$–(K-10 eV)]. The high ranking of these correlations suggests that the K-40 eV data map well to its cognate difference pairs, K-300 eV and K-500 eV where $\Delta f(\lambda) = 0$, meaning that the signal intensities of the ΔPDF pair must be comparable; yet, the second highest ranked correlation indicated that $\Delta f \neq 0$ for the K-40 eV data set. Taking these two factors into account, the prevailing assumption must be that $\Delta f(K\text{-}10\,\text{eV}) \gg \Delta f(K\text{-}40\,\text{eV})$ and that $\Delta f(K\text{-}40\ \text{eV})$ is a small but not a negligible quantity. The fifth and sixth highest ranked correlations are also related, and assess the level of similarity between ΔPDF [$E_{\text{far from edge}}$–(K-10 eV)] and ΔPDF [$E_{\text{far from edge}}$–(K-40 eV)], i.e., the cognate pairs of data collected at x-ray energies far from and on the Gd K edge, where the two energies on the edge are cross-correlated. These are on the order of 50% correlated, based on the Pearson and Spearman coefficients. Contrasting this with the 80% correlation observed between the ΔPDF [$E_{\text{far from edge}}$–(K-10 eV)] cognate pairs, these fifth and sixth-ranked coefficients effectively measure the cross correlation between the K-10 eV and K-40 eV. As was indicated in discussions above, $\Delta f(K\text{-}10\,\text{eV}) \gg \Delta f(K\text{-}40\,\text{eV})$. So, this drop in correlation by 30% presents a measure of this inequality.

There is a distinct drop in coefficient value between this pair of fifth and sixth highest ranked correlations and the next two (seventh and eighth) highest ranked correlations. These present the two-way cross correlation, comparing ΔPDF [(K-300 eV)–$E_{\text{on the edge}}$] against ΔPDF [(K-500 eV)–$E_{\text{on the edge}}$], where $E_{\text{on the edge}}$ for each comparison pair corresponds to a *mix* of the K-10 eV and K-40 eV data sets. Given that no subtraction components have a single energy in common, their coefficients are both, not surprisingly, comparable to noise levels: ±30% correlation, as judged by the coefficients that involve ΔPDF [(K-500 eV)–(K-300 eV)] for which $\Delta f = 0$, so any ΔPDF correlating against this one will be comparing against noise; see the consistently low values of coefficients in the right-hand column of Table I.

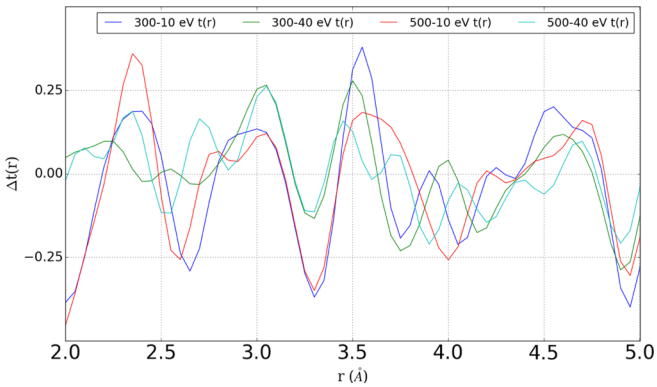

FIG. 5. ΔPDFs of the four sets of AXS signal occurring in the range $r = 2$–5 Å.

In summary, these statistical findings are as expected, with ΔPDF [$E_{\text{far from edge}}$–(K-10 eV)] signatures exhibiting the largest AXS signal, while ΔPDF [$E_{\text{far from edge}}$–(K-40 eV)] profiles showing a modest but significant AXS contribution. All other ΔPDF pairings of data acquired at the four x-ray energies manifest negligible AXS signal.

These four ΔPDF data sets that display confirmed AXS signal were taken forward as the essential results of this work, wherefrom $R \cdots X$ pairwise correlations were determined.

As an aside, the same procedure described in this section was replicated for ΔPDFs generated from subtractions, $\Delta S(Q)$, followed by the Fourier transform, for the purposes of comparison. Results shown in the Supplemental Material [65] confirm the same trend, albeit slightly weaker than that shown here. This is presumably because performing subtractions for ΔPDFs after the transforms allows for a higher Q_{max} to be used, by minimizing noise in the raw data.

V. SCIENTIFIC RESULTS

A. Determining $R \cdots X$ correlations from difference pair-distribution functions

Figures 5 and 6 show overlays of the four ΔPDF signatures that feature confirmed AXS signal, across two distinct regions

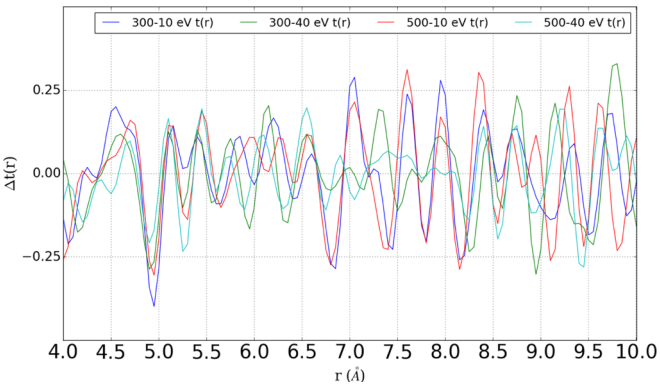

FIG. 6. ΔPDFs of the four sets of AXS signal occurring in the range $r = 4$–10 Å.

of r: 2–5 and 4−10 Å, respectively. These data have been partitioned into these two specific regions in order to distinguish structural information that displays $R \cdots X$ correlations whose average separation, $r < 4$ Å, is too low for $X = R$ (Fig. 5), from that which contain $R \cdots X$ correlations that must involve the $R \cdots R$ separations sought by this AXS study (Fig. 6). The region $4 < r < 5$ Å is shown in both Figs. 5 and 6, providing overlap between plots to help compare the two profiles.

All four data sets containing AXS signal are presented, rather than just showing the two with largest AXS signal, since all four signals are weak by virtue of being a difference PDF from the diffuse scattering associated with an amorphous material. Moreover, the overarching consideration of the challenging nature of an AXS experiment and its associated data analysis should be remembered. Accordingly, it was deemed important to display together all four sets of AXS signal, which should present the same AXS signature. Since the results manifest with low signal-to-noise, greater confidence was given to peaks that were present in all four data sets to represent real structural correlations. Peaks from the two strongest AXS signals that overlap with each other, cf. those that involve K-10 eV data, but do not correlate with peaks in the cognate K-40 eV pair of data, are nevertheless also considered. Conversely, peak overlap present only in the two AXS signatures that involve K-40 eV data ought not to be considered unless there is independent scientific support for making an exception.

Figure 5 should contain $R \cdots X$ (X = P, O) correlations that have already been observed in previous conventional diffraction studies on REPGs [12–20], where the modeling of atomic pairwise correlations could account for all structural features in the PDF up to $r \sim 4$ Å. Based on those results, selecting the case where a Gd phosphate glass of a very similar composition ($x = 0.229$) to the subject sample ($x = 0.230$) was studied [14], the following Gd $\cdots X$ correlations should be present in the ΔPDF shown in Fig. 5: Gd-O at 2.30(2) Å; Gd-(O)-P at 3.64(1) Å. Encouragingly, the ΔPDFs provide definitive evidence for these two pairwise correlations, via the consistent reproduction of peaks at these $R \cdots X$ separations across three or four ΔPDF signatures, respectively. This corroboration between the ΔPDF peak assignments in Fig. 5 and those from previous conventional diffraction data provide more direct assurance regarding the quality of the AXS data and the analysis methods that afforded them. Moreover, a statistical uncertainty of $\Delta r = 0.1$ Å was estimated from the spread of peak values observed between the regions of these ΔPDF profiles that reveal a confirmed pairwise correlation.

Figure 6 shows the potentially more exciting data since the ΔPDFs therein contain $R \cdots X$ correlations in the region beyond $r \sim 4$ Å where we anticipate evidence for $R \cdots R$ separations, the nearest of which was considered sufficiently

TABLE II. Minimum $R \cdots R$ separations found in crystal structures of rare-earth meta- and ultraphosphates, together with their associated crystallographic space group designations which help identify structural polymorphs and phase transitions as a function of increasing rare-earth atomic number, Z_R. Those for Gd are shaded in gray as the subject study focuses on this rare-earth.

Rare-earth metaphosphate crystals			Rare-earth ultraphosphate crystals		
R [Ref.]	min $R \cdots R$ (Å)	Space group	R [Ref.]	min $R \cdots R$ (Å)	Space group
La [66]	4.315	*C222(1)*	La [67]	5.246	*P2(1)/c*
Ce [68]	4.287	*C222(1)*	La [69]	5.242	*Pmna*
Ce [70]	4.281	*C222(1)*	Ce [71]	5.223	*P2(1)/c*
Pr [72]	4.253	*C222(1)*	Ce [73]	5.227	*Pmna*
Nd [33]	4.234	*C222(1)*	Pr [74]	5.205	*P2(1)/c*
Gd [75]	4.174	*C222(1)*	Nd [33]	5.197	*P2(1)/c*
Gd [76]	5.287	*I2/a*	Nd [77]	5.195	*P2(1)/c*
Tb [78]	5.255	*I2/a*	Nd [79]	5.210	*Pncm*
Dy [76]	5.659	*Cc*	Nd [80]	5.192	*Pmna*
Dy [78]	5.657	*P2(1)/c*	Sm [34]	5.175	*P2(1)/b*
Ho [78]	5.635	*P2(1)/c*	Eu [67]	5.174	*P2(1)/c*
Er [78]	5.618	*P2(1)/c*	Gd [81]	5.153	*P2(1)/a*
Er [82]	5.402	*Pm*	Gd [67]	5.171	*P2(1)/c*
Er [83]	5.640	*Ia*	Gd [84]	5.163	*P2(1)/c*
Tm [78]	5.615	*P2(1)/c*	Gd [80]	5.156	*Pmna*
Yb [85]	5.537	*P2(1)/c*	Tb [86]	5.148	*P2(1)/c*
Yb [87]	5.333	*R-3*	Dy [88]	5.710	*C2/c*
Lu [76]	5.597	*Cc*	Ho [89]	5.714	*C2/c*
			Er [90]	5.699	*C2/c*
			Er [91]	5.690	*C2/c*
			Er [92]	5.515	*Pnma*
			Er [93]	5.547	*Pnma*
			Tm [94]	5.698	*C2/c*
			Yb [95]	5.685	*C2/c*
			Lu [96]	5.703	*C2/c*

important from a materials-centered perspective to motivate this AXS study. Definite peaks from $R\cdots X$ correlations at 5.1(1) and 5.4(1) Å are indicated by the good peak overlap of their AXS signal from all four data sets. Other peaks are suggested at 4.8(1), 6.6(1), 7.1(1), 7.6(1), 7.9(1), 8.4(1), and 8.7(1) Å; their invariance in r with changing $Q_{\max}$ (see Supplemental Material [65]) suggests that they represent true local structure.

The two definitive peaks centered at 5.1(1) and 5.4(1) Å are assigned to nearest-neighbor $R\cdots R$ correlations since they match well the minimum $R\cdots R$ separations of 5.1 and 5.3 Å in crystal structures of gadolinium ultraphosphate and gadolinium metaphosphate, respectively; see reference values in Table II. The presentation of such separations from these two crystal structure archetypes adds weight to the argument advocated in Sec. II that these REPGs possess mixed ultra- and metaphosphate structural character. Moreover, the peak at 5.1(1) Å overlaps with the Sm $\cdots$ Sm correlation range of the near-ultraphosphate REPG discerned by the anomalous neutron-scattering study [27], while the peak at 5.4(1) Å lies within the broad distribution of Tb $\cdots$ Tb separations in the REPG with metaphosphate composition discovered by the magnetic difference neutron-scattering study [26]. In other words, the mixed ultra- and metaphosphate character signified by the 5.1(1) and 5.4(1) Å peak in this AXS study is wholly consistent with both glassy and crystalline structural data of rare-earth ultra- and metaphosphates.

Previous attempts to determine $R\cdots R$ separations in terbium metaphosphate glass also revealed a weak pairwise correlation at ∼4 Å. A similarly weak structural signature is potentially present in this AXS data at a slightly larger $r\sim$ 4.2 Å, if the ΔPDFs involving K-10 eV data are considered as providing the primarily representative AXS signal; tentative evidence for such a correlation also exists in the ΔPDFs involving K-40 eV data, but at a slightly larger distance of ∼4.3 Å. One might have ignored such a weak feature in this AXS signal except that it manifests as a shoulder to the larger and broader peak centered at 4.8 Å in all four cases; additionally, this weak correlation at 4.2(1) Å also presented as a peak shoulder in the previously reported evidence for this minimum $R\cdots R$ separation [26,27]. Moreover, there is a marked commonality of this asymmetric peak profile across all four ΔPDFs in this AXS study, especially considering that there are no other asymmetric double-peak profiles that are present in all four ΔPDF signatures in any other region of r; rather, the peaks in these ΔPDFs tend to be quite Gaussian in form. It is interesting that the ΔPDFs involving the K-10 eV data indicate that this suspected weak pairwise correlation is centered at $r\sim$ 4.2 Å, rather than at $r\sim$ 4.0 Å as judged by the previous evidence that exhibited lower atomic resolution. A minimum $R\cdots R$ separation of $r\sim$ 4.2 Å does in fact correspond better to that observed in $R(PO_3)_3$ crystal structures where the rare-earth atomic number $Z_R\leqslant$ Gd.

Note that the herein assignment of $R\cdots R$ separations at 4.2(1) and 5.4(1) Å means that the subject sample accommodates the two possible minimum $R\cdots R$ separations in $Gd(PO_3)_3$ crystal structures (see Table II), since gadolinium metaphosphate exhibits structural polymorphism. Table II also shows that Gd lies at a transition of commensurate structural types, as a function of the lanthanide series, whereby the minimum $R\cdots R$ separation for $R(PO_3)_3$ crystal structures is 4.2−4.3 Å for $Z_R\leqslant$ Gd and 5.3−5.7 Å for $Z_R\geqslant$ Gd. Moreover, rare-earth metaphosphates whose $Z_R\geqslant$ Tb have been shown to form incommensurate structures; in contrast, crystalline $Gd(PO_3)_3$ forms commensurate extended frameworks, which nonetheless display crystallographic superstructures [76]. Since crystallographic polymorphism occurs when multiple low-energy configurations of a structure can coexist, there is plenty of opportunity for amorphous gadolinium metaphosphate to form with the multiple low-energy structural attributes of crystalline $Gd(PO_3)_3$, as these AXS results manifest in terms of $R\cdots R$ separations.

Considering the main peak of this asymmetric double-peak profile in the ΔPDFs of these AXS results, its center ($r\sim$ 4.8 Å) is mirrored by that of the wide distribution of the Sm $\cdots$ Sm correlations observed in the amorphous rare-earth phosphate structure that was determined by anomalous neutron scattering [27]. Given that the rare-earth composition of that samarium phosphate glass ($x=0.205$) also lies between ultraphosphate and metaphosphate, and yet is closer to ultraphosphate, the reproducibility of this correlation in these AXS results is further corroboratory evidence that the subject material presents with mixed ultra- and metaphosphate structural character.

The peak centered at 4.8 Å in this AXS study nonetheless drops off with increasing r much sharper than that observed in the anomalous neutron-scattering study, where it tails off at $r\sim$ 5.5 Å. Given that this AXS study has resolved two pairwise correlations centered at 5.1 and 5.4 Å, the latter of which tails off at 5.5 Å, it would seem that the broader peak signature centered at 4.8 Å in the anomalous neutron-scattering study envelops these two correlations as well as the prominent structural signature that produces its peak center at 4.8 Å.

The next possible pairwise correlation observed with increasing r in this AXS study is centered at 6.6(1) Å. This corresponds well to the second-neighbor $R\cdots R$ correlation for a rare-earth metaphosphate glass, as observed for the case of terbium, where Tb $\cdots$ Tb separations have been observed between 6.0 and 6.4 Å by multiple methods: magnetic difference neutron scattering (6.4 Å); reverse Monte Carlo (6.4 Å); molecular-dynamics simulations (6.0 Å); first sharp diffraction peak signatures in conventional diffraction data (6.0–6.4 Å).

Without such corroboratory evidence from multiple methods, it would have been difficult to assign this peak centered at 6.6(1) Å in the AXS data, since a range of $R\cdots X$ ($X=R$, P, O) pairwise correlations could have otherwise been potentially responsible for such a peak at these larger values of r. Indeed, unambiguous peak assignments beyond this value of r are difficult given the increasing number of second-, third-, and higher-neighbor $R\cdots X$ ($X=R$, P, O) correlations that will exist and increasingly overlap.

That said, the fact that no $R\cdots X$ ($X=$ P, O) correlations show up in the region where $R\cdots R$ correlations persist, i.e., within the range of $r=4-7$ Å, tends to suggest that only structural features belonging to $R\cdots R$ correlations will likewise be resolved beyond $r=7$ Å. Indeed, $R\cdots R$ correlations will

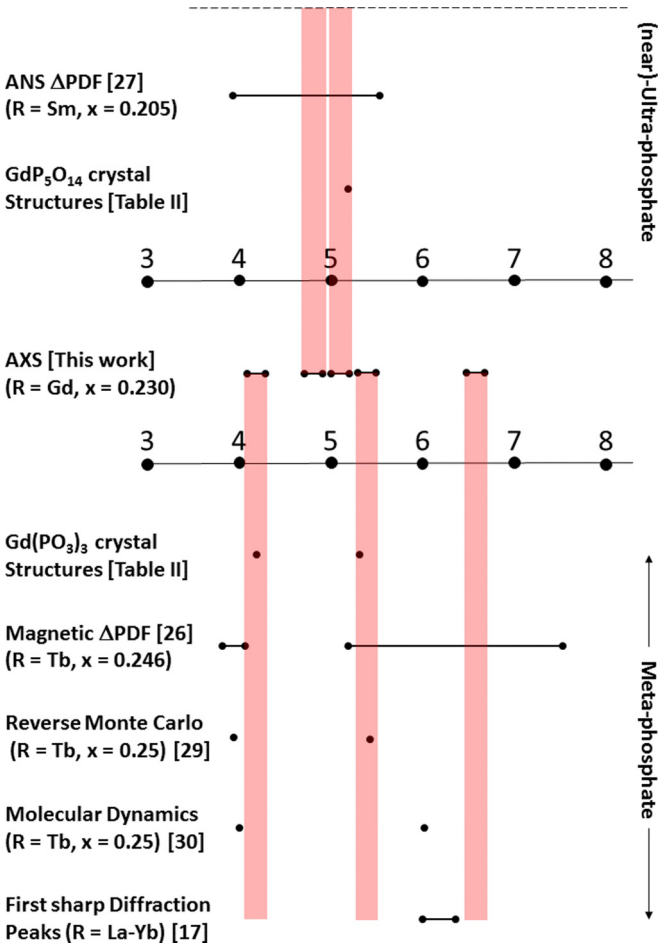

FIG. 7. $R\cdots R$ separations of the subject material determined by this AXS study, in comparison with those obtained for REPGs and their crystalline $R(PO_3)_3$ and RP_5O_{14} counterparts, using other materials characterization or computational methods.

stand out from other $R\cdots X$ correlations by virtue of the much greater strength of x-ray scattering from rare-earth elements, and because the peak heights in ΔPDFs arising from $R\cdots X$ (X = P, O) correlations will be far more diminished by large Debye-Waller factors beyond $r = 7$ Å than those of $R\cdots R$ correlations. This is simply a consequence of the fact that nth-neighbor $R\cdots R$ correlations will be of an order (n) less than that of $R\cdots X$ correlations, for a given value of r, because the size of rare-earth ions is larger than those of P and O. Thus, while the static disorder of all correlations increases with r, owing to a rise in variance of bond angles that help define these atomic separations, $R\cdots X$ (X = P, O) correlations will be affected more than $R\cdots R$ correlations for a given radial distribution, r. Nonetheless, peak assignment beyond $r = 7$ Å in this AXS study maintains the option for features to belong to any of the three types of $R\cdots X$ ($X = R$, P, O) correlation.

To this end, the possible correlations shown at 7.1(1), 7.6(1), and 7.9(1) Å in these AXS data are now considered. That at 7.1(1) Å lies within the broad envelope of the ΔPDF distribution determined by the magnetic difference neutron-scattering experiment on terbium metaphosphate glass. The tail of that broad envelope could conceivably contain the peak centered at 7.6(1) Å indicated by this AXS study, although interpreting data within the tail of such a distribution is tricky, especially given that the resolution in that previous study is so low. The resolution of this AXS study is much higher and so this peak at 7.6(1) Å presents the first significant indication of an $R\cdots X$ correlation at this value of r. The peak at 7.9(1) Å is likewise first suggested by this AXS study. The presence of a broad distribution of $R\cdots X$ correlations in rare-earth metaphosphate glasses, covering the range ∼7.5−9.0 Å, has nonetheless been suggested previously via a conventional x-ray diffraction study [17]. So, this distribution could conceivably contain the correlation at 7.9(1) Å observed by this AXS study.

The same distribution could also contain the two other possible correlations noted by this AXS study which lie at 8.4(1) and 8.7(1) Å. These correlations are more directly corroborated by the broad, but fairly assured, correlation centered at 8.8 Å evidenced by the anomalous neutron-scattering study to represent $R\cdots R$ separations. The two possible $R\cdots X$ correlations seen in this AXS study are resolved and appear to be real, as judged by the entirely consistent peak overlap at 8.4(1) and 8.7(1) Å in the ΔPDFs from all four AXS data sets. These were the last two possible pairwise correlations considered in this AXS study, owing to difficulties in consistency between ΔPDF peak signatures observed beyond $r \sim 9$ Å (see Fig. 6).

An overarching model of $R\cdots X$ correlations for the gadolinium phosphate glass has been produced from these peak assignments. The assignments comprising $R\cdots R$ separations have been corroborated by cognate sets of structural data on REPGs or rare-earth meta- or ultraphosphate crystal structures. Results show that the local structure of gadolinium phosphate glass contains multiple rare-earth ion environments, with manifold $R\cdots R$ separations representing a mix of archetypal meta- and ultraphosphate structural characteristics. This is presumably because the rare-earth composition of the subject material lies between meta- and ultraphosphate ($x = 0.230$). The $R\cdots R$ separations determined by this AXS study are consistent with those obtained by other methods, as summarized by Fig. 7.

VI. CONCLUSIONS

The AXS results presented in this study, in corroboration with findings from other studies, evidence that rare-earth phosphate glasses show mixed ultra- and metaphosphate structural character, where their rare-earth composition lies between the two stoichiometric boundaries of RP_5O_{14} ($x = 0.167$) and $R(PO_3)_3$ ($x = 0.250$). The AXS data comprise difference pair-distribution functions of $R\cdots X$ correlations ($X = R$, P, O) for a gadolinium phosphate glass ($x = 0.230$). $R\cdots R$ pairwise correlations in its amorphous structure have been assigned on the basis of consistency with $R\cdots R$ separations in other REPGs determined by the two difference neutron-scattering studies on REPGs [26,27], conventional diffraction studies that indicate first sharp diffraction peaks [17], and supporting computational studies from reverse Monte Carlo [29] and molecular-dynamics [30] simulations as well as comparing them against minimum $R\cdots R$ separations observed in rare-earth ultra- and metaphosphate crystal structures (see Table II). On the one hand, our findings have confirmed previous peak

assignments and related certain $R \cdots R$ correlations to archetypal meta- or ultraphosphate structural characteristics: 4.2(1) Å (meta), 4.8(1) Å (ultra/meta), 5.1(1) Å (ultra), 5.4(1) Å (meta), and 6.6(1) Å (meta). On the other hand, our AXS results have provided resolved peak signatures of $R \cdots X$ correlations that lie at average separations of 7.1(1), 7.6(1), 7.9(1), 8.4(1), and 8.7(1) Å. These separations could only be classified and quantified by virtue of the high spatial resolution enabled by anomalous x-ray scattering at energies in the region of the Gd K edge, in contrast to the very broad distributions of REPG structures observed previously by the two other difference atomic-scattering studies [26,27], both of which use neutrons as the atomic probe. Moreover, the majority of the well-resolved peaks in this study were observed in all four ΔPDFs that each represent the AXS signal, as determined by subtracting x-ray diffraction data collected at an x-ray energy that lies far from the Gd K edge from a cognate data set acquired at an energy on the edge. Four x-ray energies were employed to obtain the diffraction data for these subtracted pairings, which lie at 10, 40, 300, and 500 eV from the Gd K edge; ΔPDFs involving the K-10 eV data set afforded the most intense and reliable AXS signal, as expected.

Our study is a Gd K-edge AXS report on an amorphous material which has come with a range of technical challenges, not least being the presence of inelastic x-ray scattering features that overlap in energy with Gd K_α fluorescence. This precluded the use of the data-processing methodology that is normally used to extract and isolate the AXS signal from the total scattering. Instead, a custom fitting procedure was applied to the data in this study, making careful data validation especially important at several stages of data processing. Such validation included the use of statistical correlation to compare the relative merits of the multiple AXS data signatures. The good spatial resolution of the ΔPDFs so afforded, out to a radial distribution of at least $r \sim 9$ Å, demonstrates exciting prospects for future AXS studies on other amorphous materials which are at least ternary in nature.

ACKNOWLEDGMENTS

J.M.C. is grateful to the Royal Commission of the Great Exhibition 1851 for a 2014 Design Fellowship hosted by Argonne National Laboratory (ANL) where work done was supported by the U.S. Department of Energy (DOE) Office of Science, Office of Basic Energy Sciences, and X-ray 1-BM beam line of the Advanced Photon Source, which is a DOE Office of Science User Facility, all under Contract No. DE-AC02-06CH11357. J.M.C. and R.J.N. are also indebted to the Engineering and Physical Sciences Research Council Grant No. GR/L41035 for funding. We thank Tessa Brennan and George A. Saunders for sample provision. We also wish to thank Adrian C. Barnes (University of Bristol, United Kingdom), Dean Haeffner (Sector 1, Advanced Photon Source, ANL), David L. Price, and Marie-Louise Saboungi (formerly of ANL) for helpful discussions.

[1] M. M. Broer, A. J. Bruce, and W. H. Grodkiewicz, Phys. Rev. B **45**, 7077 (1992).
[2] G. Carini, G. D'Angelo, G. Tripodo, A. Fontana, F. Rossi, and G. A. Saunders, Europhys. Lett. **40**, 435 (1997).
[3] F. M. Durville, E. G. Behrens, and R. C. Powell, Phys. Rev. B **34**, 4213 (1986).
[4] D. B. He, C. L. Yu, J. M. Cheng, S. G. Li, and L. L. Hu, Chin. Phys. Lett. **27**, 114208 (2010).
[5] X. Liang, Z. Chaofeng, Y. Yang, S. Yuan, and G. Chen, J. Lumin. **128**, 1162 (2008).
[6] R. A. Martin and J. C. Knight, IEEE Photon. Technol. Lett. **18**, 574 (2006).
[7] L. Zhang, H. Hu, C. Qi, and F. Lin, Opt. Mater. **17**, 371 (2001).
[8] P. Laporta, S. Taccheo, S. Longhi, O. Svelto, and G. Sacchi, Opt. Lett. **18**, 1232 (1993).
[9] G. A. Saunders, T. Brennan, M. Acet, M. Cankurtaran, H. B. Senin, H. A. A. Sidek, and M. Federico, J. Non-Cryst. Solids **282**, 291 (2001).
[10] H. M. Farok, H. B. Senin, G. A. Saunders, W. Poon, and H. Vass, J. Mater. Sci. **29**, 2847 (1994).
[11] P. J. Ford, C. D. Graham, G. A. Saunders, H. B. Senin, and J. R. Cooper, J. Mater. Sci. Lett. **13**, 697 (1994).
[12] D. T. Bowron, R. J. Newport, B. D. Rainford, G. A. Saunders, and H. B. Senin, Phys. Rev. B **51**, 5739 (1995).
[13] U. Hoppe, R. Kranold, D. Stachel, A. Barz, and A. C. Hannon, J. Non-Cryst. Solids **232–234**, 44 (1998).
[14] J. M. Cole, E. R. H. van Eck, G. Mountjoy, R. Anderson, T. Brennan, G. Bushnell-Wye, R. J. Newport, and G. A. Saunders, J. Phys.: Condens. Matter **13**, 4105 (2001).
[15] U. Hoppe, H. Ebendorff-Heidepriem, J. Neuefeind, and D. T. Bowron, Z. Naturforsch. A **56**, 237 (2001).
[16] U. Hoppe, E. Metwalli, R. K. Brow, and J. Neuefeind, J. Non-Cryst. Solids **297**, 263 (2002).
[17] U. Hoppe, R. K. Brow, D. Ilieva, P. Jóvári, and A. C. Hannon, J. Non-Cryst. Solids **351**, 3179 (2005).
[18] U. Hoppe, N. P. Wyckoff, R. K. Brow, and U. Rütt, J. Non-Cryst. Solids **357**, 2516 (2011).
[19] A. J. Cramer, J. M. Cole, R. J. Newport, V. FitzGerald, V. Honkimaki, M. A. Roberts, T. Brennan, R. A. Martin, and G. A. Saunders, Phys. Chem. Chem. Phys. **15**, 8529 (2013).
[20] J. M. Cole, E. R. H. van Eck, G. Mountjoy, R. J. Newport, T. Brennan, and G. A. Saunders, J. Phys.: Condens. Matter **11**, 9165 (1999).
[21] J. M. Cole, R. J. Newport, D. T. Bowron, R. F. Pettifer, G. Mountjoy, T. Brennan, and G. A. Saunders, J. Phys.: Condens. Matter **13**, 6659 (2001).
[22] R. Anderson, T. Brennan, J. M. Cole, G. Mountjoy, D. M. Pickup, R. J. Newport, and G. A. Saunders, J. Mater. Res. **14**, 4706 (1999).
[23] G. Mountjoy, J. M. Cole, T. Brennan, R. J. Newport, G. A. Saunders, and G. W. Wallidge, J. Non-Cryst. Solids **279**, 20 (2001).
[24] D. T. Bowron, G. A. Saunders, R. J. Newport, B. D. Rainford, and H. B. Senin, Phys. Rev. B **53**, 5268 (1996).
[25] D. Ilieva, D. Kovacheva, J. M. Cole, and I. Gutzow, Phosphorus Res. Bull. **13**, 137 (2002).
[26] J. M. Cole, A. C. Hannon, R. A. Martin, and R. J. Newport, Phys. Rev. B **73**, 104210 (2006).

[27] J. M. Cole, A. C. Wright, R. J. Newport, C. E. Fisher, S. J. Clarke, R. N. Sinclair, H. E. Fisher, and G. J. Cuello, J. Phys.: Condens. Matter **19**, 056002 (2007).

[28] A. C. Wright, J. M. Cole, R. J. Newport, C. E. Fisher, S. J. Clarke, R. N. Sinclair, H. E. Fisher, and G. J. Cuello, Nucl. Instrum. Methods **571**, 622 (2007).

[29] G. Mountjoy, R. Anderson, D. T. Bowron, and R. J. Newport, J. Non-Cryst. Solids **232–234**, 227 (1998).

[30] E. B. Clark, R. N. Mead, and G. Mountjoy, J. Phys.: Condens. Matter **18**, 6815 (2006).

[31] R. N. Sinclair, in *Proceedings of the ILL/ESRF Workshop on Methods in the Determination of Partial Structure Factors of Disordered Matter by Neutron and Anomalous X-ray Diffraction*, edited by J. B. Suck, D. Raoux, P. Chieux, and C. Riekel (World Scientific, Singapore, 1993), p. 107.

[32] J. M. Cole, L. Ward, M. A. Roberts, D. Ilieva, C. Wolverton, and R. J. Newport (unpublished).

[33] H. Y.-P. Hong, Acta Cryst. B **30**, 468 (1974).

[34] D. Tranqui, M. Bagieu, and A. Durif, Acta Cryst. B **30**, 1751 (1974).

[35] J. Krogh-Moe, Acta Chem. Scand. **20**, 2890 (1966).

[36] D. L. Price, M.-L. Saboungi, and A. C. Barnes, Phys. Rev. Lett. **81**, 3207 (1998).

[37] C. Meneghini, A. Balerna, F. Boscherini, S. Pascarelli, and S. Mobilio, J. Synchrotron Radiat. **5**, 1258 (1998).

[38] P. H. Fuoss, P. Eisenberger, W. K. Warburton, and A. Bienenstock, Phys. Rev. Lett. **46**, 1537 (1981).

[39] S. Hosokawa, J. R. Stellhorn, W.-C. Pilgrim, and J.-F. Bérar, Z. Phys. Chem. **230**, 313 (2016).

[40] S. Ramos, G. W. Neilson, A. C. Barnes, and P. Buchanan, J. Chem. Phys. **123**, 214501 (2005).

[41] S. Ramos, G. W. Neilson, A. C. Barnes, and M. J. Capitán, J. Chem. Phys. **118**, 5542 (2003).

[42] S. Ramos, G. W. Neilson, A. C. Barnes, and A. Mazuelas, J. Phys. Chem. B **105**, 2694 (2001).

[43] S. Ramos, A. C. Barnes, G. W. Neilson, D. Thiaudiere, and S. Lequien, J. Phys.: Condens. Matter **11**, A203 (1999).

[44] E. Matsubara, Y. Waseda, A. Inoue, H. Ohtera, and T. Masumoto, Z. Naturforsch. A **44**, 814 (1989).

[45] M. Saito, Y. Waseda, E. Matsubara, X.-M. Wang, T. Aihara, K. Aoki, and T. Masumoto, J. Non-Cryst. Solids **205–207**, 721 (1996).

[46] V. Petkov and S. D. Shastri, Phys. Rev. B **81**, 165428 (2010).

[47] R. W. James, *The Optical Principles of the Diffraction of X-rays* (G. Bell and Sons, London, 1962).

[48] R. D. L. Kronig, J. Opt. Soc. Am. **12**, 547 (1926).

[49] H. A. Kramers, Atti Cong. Intern. Fisica, Transactions of Volta Centenary Congress, Como **2**, 545 (1927).

[50] S. Hosokawa, I. Oh, M. Sakurai, W.-C. Pilgrim, N. Boudet, J.-F. Bérar, and S. Kohara, Phys. Rev. B **84**, 014201 (2011).

[51] D. B. Tanner, Phys. Rev. B **91**, 035123 (2015).

[52] Y. Waseda, *Anomalous X-ray Scattering for Materials Characterization* (Springer-Verlag, Heidelberg, 2002).

[53] Y. Waseda, *Novel Application of Anomalous (Resonance) X-ray Scattering for Structural Characterization of Disordered Materials* (Springer-Verlag, Heidelberg, 1984).

[54] H. Oyanagi, M. Martini, and M. Saito, Nucl. Instrum. Methods A **403**, 58 (1998).

[55] R. D. Deslattes, E. G. Kessler, Jr., P. Indelicato, L. de Billy, E. Lindroth, and J. Anton, Rev. Mod. Phys. **75**, 35 (2003).

[56] A. Mierzejewski, G. A. Saunders, H. A. A. Sidek, and B. Bridge, J. Non-Cryst. Solids **104**, 323 (1988).

[57] T. Brennan, Ph.D. thesis, University of Bath (UK), 1998.

[58] G. Evans and R. F. Pettifer, J. Appl. Crystallogr. **34**, 82 (2001).

[59] W. H. McMaster, N. Kerr del Grande, J. H. Mallett, and J. H. Hubbell, *Compilation of X-ray Cross Sections*. Tech. Rep. UCRL-50174 Section II Revision I (Lawrence Livermore National Laboratory, Livermore, CA, 1969), p. 129.

[60] M. O. Krause and J. H. Oliver, J. Phys. Chem. Ref. Data **8**, 329 (1979).

[61] J. A. Bearden, Rev. Mod. Phys. **39**, 78 (1967).

[62] M. Wojdyr, J. Appl. Crystallogr. **43**, 1126 (2010).

[63] P. H. Gaskell, in *Materials Science and Technology Volume 9: Glasses and Amorphous Materials*, edited by J. Zrzycky (Wiley-VCH, Weinheim, 1991), Chap. 4.

[64] B. Everitt and A. Skronda, *The Cambridge Dictionary of Statistics*, 4th ed. (Cambridge University Press, Cambridge, 2011).

[65] See Supplemental Material at http://link.aps.org/supplemental/10.1103/PhysRevMaterials.2.045604 for ΔPDFs created by subtracting $S(Q)$ signals from different x-ray energies prior to performing a Fourier transform; and difference pair-distribution functions with varying $Q_{\max}$.

[66] J. Matuszewski, J. Kropiwnicka, and T. Znamierowska, J. Solid State Chem. **75**, 285 (1988).

[67] J. M. Cole, M. R. Lees, J. A. K. Howard, R. J. Newport, G. A. Saunders, and E. Schönherr, J. Solid State Chem. **150**, 377 (2000).

[68] H. N. Tong, H. Zhang, W. D. Cheng, D. S. Wu, Y. J. Gong, J. Zhu, S. P. Huang, and D. Zhao, Jiegou Huaxue **26**, 338 (2007).

[69] J. Zhu, H. Chen, Y. D. Wang, S. Zhang, W. D. Cheng, and H. T. Guan, Chin. J. Struc. Chem. **30**, 648 (2011).

[70] J. M. Cole and D. Ilieva, Acta Cryst. Sect. E **63**, i138 (2007).

[71] M. Mesfar, M. Abdelhedi, M. Dammak, and M. Ferid, J. Mol. Struct. **1028**, 196 (2012).

[72] A. Jouini, M. Ferid, J.-C. Gâcon, L. Grosvalet, A. Thozet, and M. Trabelsi-Ayadi, Mater. Res. Bull. **38**, 1613 (2003).

[73] J. Zhu, W.-D. Cheng, and H. Zhang, Acta Cryst. Sect. E **64**, i74 (2008).

[74] S. Liu, G. Hong, and N. Hu, Wu Li Hsueh Pao **40**, 64 (1991).

[75] H. Naïli, H. Ettis, S. Yahyaoui, and T. Mhiri, Mater. Res. Bull. **41**, 1990 (2006).

[76] H. A. Höppe and S. Sedlmaier, Inorg. Chem. **46**, 3467 (2007).

[77] K.-R. Albrand, R. Attig, J. Fenner, J. P. Jeser, and D. Mootz, Mater. Res. Bull. **9**, 129 (1974).

[78] H. A. Höppe, J. Solid State Chem. **182**, 1786 (2009).

[79] H. Schulz, K.-H. Thiemann, and J. Fenner, Mater. Res. Bull. **9**, 1525 (1974).

[80] A. J. Cramer and J. M. Cole (unpublished).

[81] Y.-H. Lin, N.-H. Hu, Q.-G. Zhou, and S.-X. Wu, Chin. J. Appl. Chem. **0**(1), 33 (1983).

[82] G. I. Dorokhova and O. G. Karpov, Kristallografiya **29**, 677 (1984).

[83] E. V. Murashova, N. N. Chudinova, and A. B. Ilyukhin, Kristallografiya **52**, 252 (2007).

[84] H. Ettis, H. Naïli, and T. Mhiri, Mater. Chem. Phys. **102**, 275 (2007).

[85] H. Y. P. Hong, Acta Cryst. Sect. B **30**, 1857 (2007).
[86] Y.-H. Lin, H. Ninghai, M.-Y. Wang, and E.-D. Shi, Hua Hsueh Hsueh Pao **40**, 211 (1982).
[87] N. Y. Anisimova, V. K. Trunov, N. B. Karmanovskaya, and N. N. Chudinova, Izv. Akad. Nauk SSSR, Neorg. Mater. **28**, 441 (1992).
[88] F. Chehimi-Moumen and M. Férid, Acta Cryst. Sect. E **63**, i89 (2007).
[89] M. Bagieu, I. Tordjman, A. Durif, and G. Bassi, Acta Crystallogr. Sect. C: Cryst. Struct. Commun. **2**, 387 (1973).
[90] B. Jezeowska-Trzebiatowska, Z. Mazurak, and T. Lis, Acta Cryst. Sect. B **36**, 1639 (1980).
[91] Y.-H. Lin, N.-H. Hu, Q.-L. Zhou, E.-D. Shi, M.-Y. Wang, S.-Z. Liu, and S.-X. Wu, K'o Hsueh T'ung Pao **27**, 281 (1982).
[92] A. Katrusiak and F. Kaczmarek, Cryst. Res. Technol. **30**, 501 (1995).
[93] O. V. Dimitrova, D. A. Ksenofontov, V. Massa, O. V. Yakubovich, and G. I. Dorokhova, Vestn. Mosk. Univ. Geol. 48 (2004).
[94] K.-J. Zhou, Y.-T. Qian, and G.-Y. Hong, Acta Crystallogr. Sect. C: Cryst. Struct. Commun. **11**, 1695 (1982).
[95] H.-P. Hong and J. W. Pierce, Mater. Res. Bull. **9**, 179 (1974).
[96] A. Gagor, A. Pietraszko, and V. V. Panko, Acta Cryst. Sect. C **64**, i33 (2008).